Materials Research Express

PAPER • **OPEN ACCESS**

Comparative investigation of friction stir welds reinforced with graphene nanoplatelets and copper in AA6082-T6 alloy

To cite this article: Rahul Biradar *et al* 2024 *Mater. Res. Express* **11** 106519

Materials Research Express

PAPER

Comparative investigation of friction stir welds reinforced with graphene nanoplatelets and copper in AA6082-T6 alloy

Rahul Biradar[1], **Sachinkumar Patil**[1,*], **Priyaranjan Sharma**[2,*] and **Filipe Fernandes**[3,4,5]

[1] School of Mechanical Engineering, REVA University, Bengaluru - 560064, Karnataka, India
[2] Department of Mechanical Engineering, Koneru Lakshmaiah Education Foundation, Vijayawada - 522502, Andhra Pradesh, India
[3] University of Coimbra, CEMMPRE, ARISE, Department of Mechanical Engineering, Rua Luís Reis Santos, 3030-788 Coimbra, Portugal
[4] CIDEM, ISEP, Polytechnic of Porto, Rua Dr António Bernardino de Almeida, 4249-015, Porto, Portugal
[5] IPN - LED&MAT - Instituto Pedro Nunes, Laboratório de Ensaios, Desgaste e Materiais, Rua Pedro Nunes, 3030-199, Coimbra, Portugal
[*] Authors to whom any correspondence should be addressed.

E-mail: sachindongapur@gmail.com **and** priya333ranjan@gmail.com

Keywords: AA6082-T6 alloy, tensile strength, friction stir welding, grain structure, graphene nanoplatelets, transmission electron microscope

OPEN ACCESS

RECEIVED
20 June 2024

REVISED
25 September 2024

ACCEPTED FOR PUBLICATION
3 October 2024

PUBLISHED
23 October 2024

Abstract

Friction stir welding (FSW) represents a solid-state welding method renowned for producing high-quality joints, particularly in aluminum alloys. This study focuses on enhancing weld strength in the aerospace alloy AA6082-T6. The research involved conducting experiments to create FSW joints in AA6082-T6 by incorporating graphene nanoplatelets (GNPs) and copper as filler materials. Various characteristics of the joints, including microhardness, tensile strength, wear resistance, and corrosion behavior, were meticulously investigated. The experimental findings demonstrated that AA6082-T6 joints reinforced with GNPs exhibited significantly higher weld strength than conventional joints. This improvement can be attributed to the superior bonding and reinforcing effects of GNPs within the aluminum matrix. Furthermore, the GNPs incorporated joints displayed enhanced electrochemical and wear properties. This innovative approach in FSW presents a promising avenue for enhancing weld strength across diverse alloys through the integration of different reinforcement materials.

1. Introduction

Aluminum-magnesium-silicon alloys, particularly the AA6082-T6 variant, are highly valued in the aerospace sector for fabricating contemporary components such as seats, fuselage tanks, wings, and missile parts [1–3]. The AA6082-T6 alloy is prominently employed in Boeing aircraft structures due to its superior properties [4, 5], characterized by excellent strength and formability. However, conventional welding methods like tungsten inert gas (TIG) and metal inert gas (MIG) often lead to defects such as porosity, cracks, slag inclusions, and surface irregularities. As a result, the effectiveness of weld joints decreases [6, 7]. Thus, these technologies are insufficient for welding aluminum alloys.

To address these challenges, researchers have turned to the friction stir welding (FSW) technique. A novel solid-state joining technique patented by The Welding Institute (TWI) U.K. in 1991 [8]. Friction stir processing (FSP) is a surface modification technique developed based on FSW [9]. This innovative approach has enabled the creation of aluminum matrix composites (AMCs) using various reinforcements such as silicon carbide (SiC), tungsten carbide (WC), boron carbide (B_4C), titanium carbide (TiC), aluminum oxide (Al_2O_3), titanium diboride (TiB_2), carbon nanotubes (CNTs), and graphene nanoplatelets (GNPs) [10, 11]. GNPs, renowned for enhancing material strength while reducing weight, offer superior mechanical properties as compared to conventional micro reinforcements [12, 13]. Recently, nano reinforcements like carbon nanotubes (CNTs) and graphene nanoplatelets (GNPs) are gaining attention due to their superior properties. GNPs provide a larger surface area and better bonding between grain boundaries. Specifically, GNPs offer greater strength and flexibility. In an aluminum matrix, they induce new deformation patterns like grain sliding and bridging. This

Table 1. Chemical composition of AA6082-T6 alloy.

Elements	Mg	Cu	Si	Mn	Fe	Zn	Cr	Ti	Mn	Al
Weight %	0.77	0.03	0.91	0.61	0.21	0.04	0.02	0.04	0.61	Remaining

Table 2. Mechanical properties of AA6082-T6 alloy.

Yield strength (MPa)	Ultimate tensile strength (MPa)	Elongation (%)
152	460	21

differs from composites with CNTs and ceramic reinforcements [14]. Notably, GNPs have been reported to contribute to a 20% reduction in fuel consumption in Boeing 787 applications [15], thanks to their high tensile strength, excellent electrical conductivity, and favorable thermal properties, which make them viable materials for several applications [16]. The GNPs are effectively contributing to weight reduction and, therefore, lowering fuel consumption, which are critical objectives in modern aviation [17]. They can effectively be utilized to decrease the weight of existing fuselage tanks for space programs and commercial aircraft such as Jet Eclipse.

In recent decades, considerable research interest has focused on investigating the mechanical and microstructural properties of friction stir welded (FSWed) joints, between similar and dissimilar alloys, with particular relevance to aircraft applications. Several noteworthy studies are discussed here. Sunil *et al* [18] used stir casting to create AA6061/GNPs composites and observed higher microhardness compared to unreinforced AA6061. Yijun *et al* [19] explored friction stir processing (FSP) of graphene/aluminum composites via *in situ* exfoliation, observing a 15% hardness improvement and confirming strong GNP-aluminum bonding through transmission electron microscopy (TEM). Sung *et al* [20] investigated AA5052-H32/AA6061-T4 dissimilar alloys reinforced with graphite powder, detecting GNPs in the nugget zone via Raman spectroscopy. Khodabakhshi *et al* [21] studied AA5052/GNPs FSP, noting GNPs secondary phase formation within weld nuggets and achieving significant enhancements in joint tensile strength (220%) and hardness (55%) after multiple passes. Shuai *et al* [22] observed graphene nanosheets forming an interlayer in FSW of AA2014/GNPs, resulting in 31% higher tensile strength and 20% improved fracture toughness. Overall, these studies underscore the beneficial role of GNPs in enhancing the weld strength of aluminum alloys. Researchers have also studied the use of copper and observed the formation of intermetallic compounds (IMCs) in the nugget zone, which leads to improved tensile strength and hardness. Here are some key findings from the literature: Syahid *et al* [23] found that adding 0.5% GNPs during friction stir welding (FSW) of copper/aluminum alloys resulted in a 15% increase in shear strength and a 46% increase in joint hardness. Sinha *et al* [24] identified IMCs such as AlCu, Al_4Cu_9, Al_2Cu, and Al_2Cu_3 at the interface and in the nugget zone of Al/Cu joints. Muthu *et al* [25] observed higher tensile strength in Al/Cu FSW joints due to the dispersion strengthening of copper in the nugget zone, with IMCs like Al_2Cu, AlCu, and Al_4Cu_9 present. Carvalho *et al* [26] reported microstructural changes in the nugget zone of Al/Cu joints due to plastic deformation, leading to increased hardness from IMCs formation. Lastly, Galvao *et al* [27] investigated Al/Cu alloys in FSW and found a lamellar structure rich in Al/Cu in the nugget zone, with IMCs such as $CuAl_2$ and Cu_9Al_4 enhancing joint efficiency. However, the systematic investigation into FSW characteristics of AA6082-T6/GNPs and AA6082-T6/Cu joints remains limited. Therefore, this current work aims to develop a novel approach to enhance the weld strength in AA6082-T6 using GNPs and Cu filler, investigating the mechanical, microstructural, wear, and electrochemical corrosion behaviors of the FSWed joints. It could emphasize the study's uniqueness, objectives, and potential influence on relevant industries.

2. Experimental procedure

In this research, an aluminum alloy of AA6082-T6 is utilized as the experimental material, sized at 100 × 50 × 6 mm^3. The material was procured from Adnano Technology Private Limited, Shivamogga, India. Tables 1 and 2 present the chemical composition and mechanical properties of AA6082-T6, respectively. The graphene nanoplatelets (GNPs) are used as filler material for the FSW process. Microscopic images of the GNPs, captured using a Scanning electron microscope (SEM) [Model: TESCAN VEGA 3 LMU], are shown in figures 1(a) and (b) at magnifications of 5000 X and 35000 X, highlighting their morphology. The GNPs are composed of multilayer graphene sheets with a platelet structure, measuring 3 to 4 nm in thickness and approximately 1 to 5 μm in

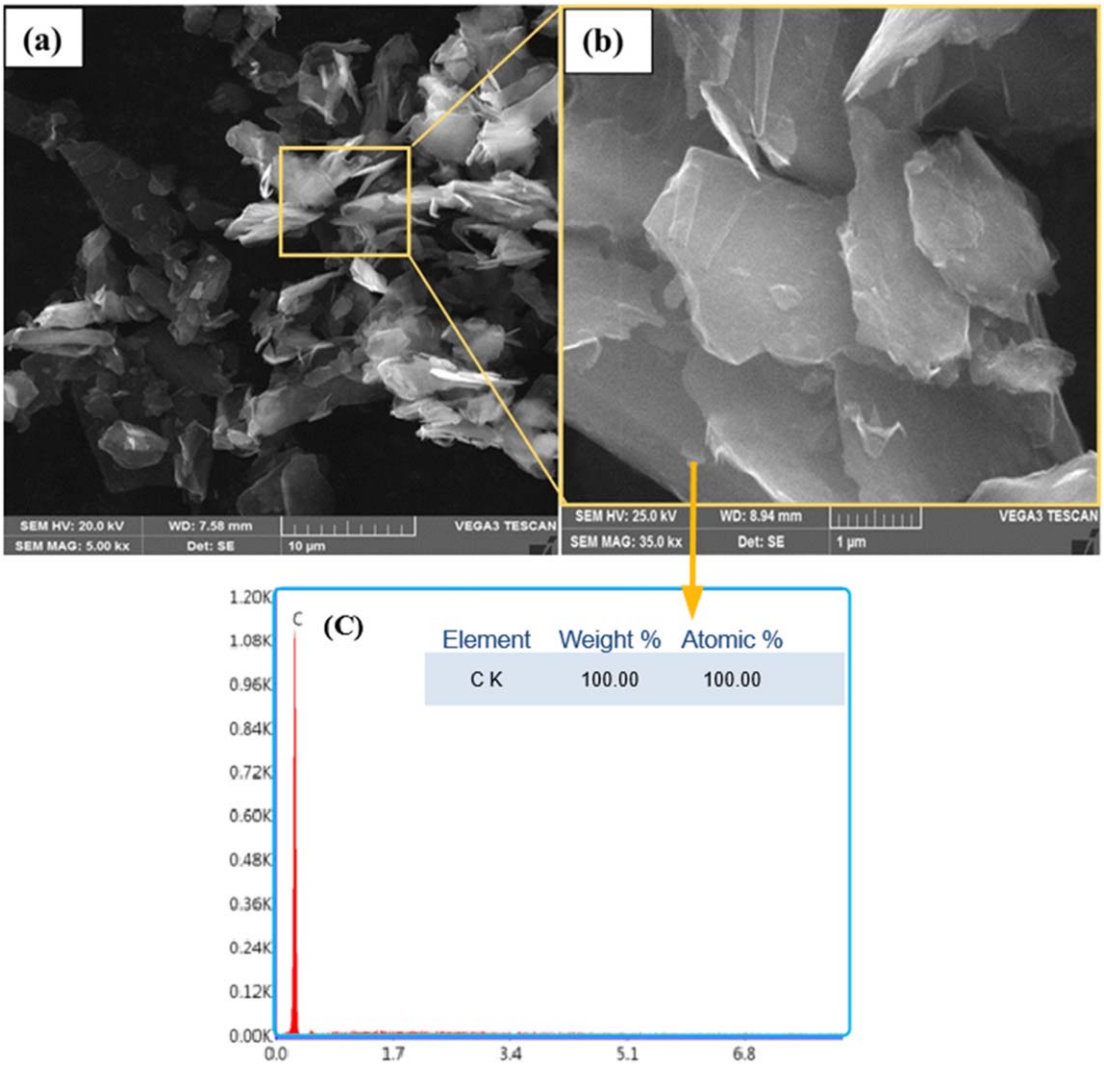

Figure 1. SEM photo micrographs of GNPs at (a) 5 kx; (b) 35 kx ; (c) EDS of GNPs.

length, as depicted in figure 1. They appear in wrinkled, curled, and overlapping forms, as illustrated in figure 1. Individual graphene layers are visible under a low accelerating voltage of 0.5 to 2.0 kV. The SEM also includes energy dispersive x-ray spectroscopy (EDS) to examine the elemental composition of the GNPs, as displayed in figure 1(c). Figure 2 presents the x-ray diffraction (XRD) pattern, obtained using a PAN analytical X'Pert3 Powder, which provides insights into the structural characteristics of the GNPs. The XRD analysis aids in determining the crystal structure and composition of the material, with diffraction peaks at 26.5°, 43.2°, 54.8°, and 72.1°, indicative of the GNPs' composition [13].

A conventional milling machine (Model: UFI, RV Machine Tools Pvt. Ltd) was used, as shown in figure 3(a). The welding tool employed with a square pin is made of H13 tool steel, measuring 6 mm on each side, with a length of 5.8 mm and shoulder diameter of 20 mm, as depicted in figure 3(b). The Wear test and tensile test setup are shown in figures 3(c) and (d), respectively. Microstructural characteristics were examined using optical microscopy (OM), SEM, and TEM analysis. The microstructure samples were initially polished using silicon carbide (SiC) emery sheets of varying grades: 100, 200, 300, and 400 µm. Following this, alumina (Al_2O_3) powder with a size of 1 µm was used for polishing. The samples were then polished with a diamond paste of ¼ µm size and diamond spray to achieve a mirror finish. Finally, the polished samples were etched for 15 s in Keller's reagent (190 ml of H_2O, 5 ml of HNO_3, 3 ml of HCl, and 2 ml of HF) to reveal their surface morphologies. Vickers microhardness analysis (Model: Wilson VH 1102) was performed using a 1 kgf load and a dwell time of 10 s with a Vickers indenter. Samples for the microhardness test were prepared following ASTM E384–11E1 standards, and the tensile test was performed using a TUF-C-1000 kN machine in accordance with ASTM E8 standards. The electrochemical corrosion study was performed at room temperature using 3.5 wt% of NaCl solution, and an analysis of electrochemical parameters was carried out using ZSimpWin software. Additionally, TEM analysis (Model: Titan Themis 300 kV FEI Thermo) was conducted to examine the microstructural

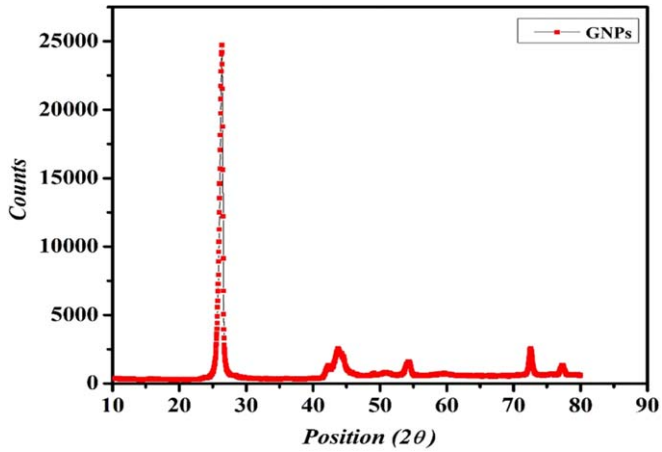

Figure 2. XRD pattern of GNPs.

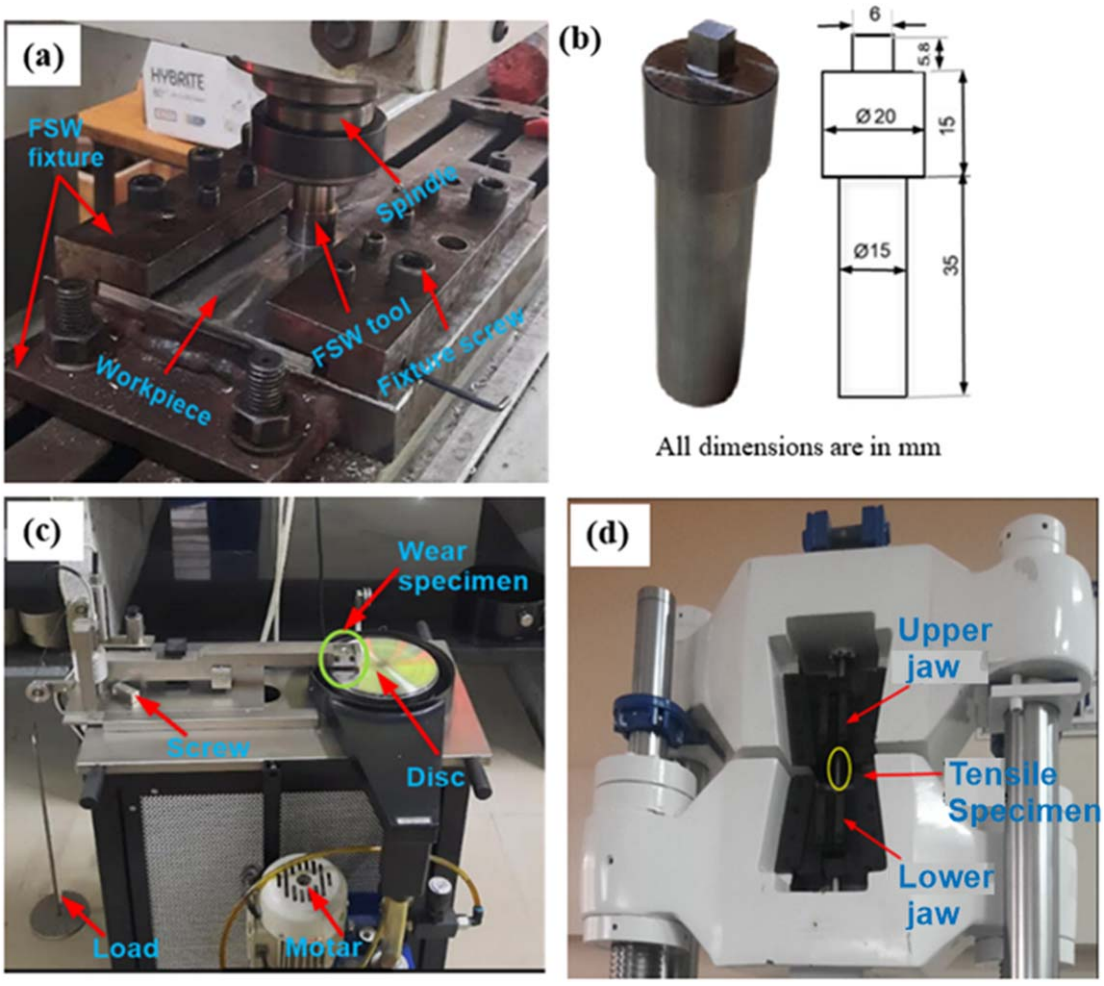

Figure 3. Experiments are carried out at (a) FSW setup; (b) FSW tool; (c) Pin on disc wear test setup; (d) Tensile test setup.

features at the nanoscale, enabling detailed observation of dislocations in the welded regions. TEM specimens were sliced to 60 nm thickness using the focused ion beam (FIB) technique, placed into 3 mm diameter holders, and then prepared in a 25% HNO_3 methanol solution at −30°C using the twin jet electropolishing technique. Furthermore, a pin-on-disc wear setup (Model: Ducom TR 20LE) was utilized for the experimental investigation.

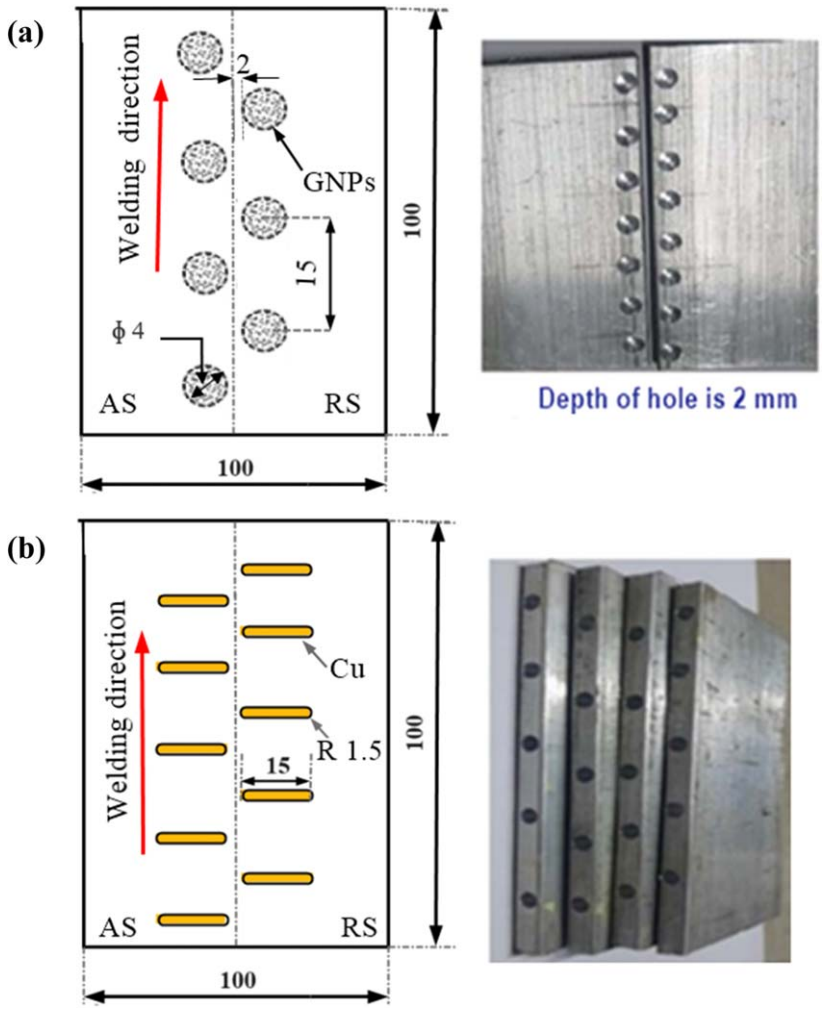

Figure 4. Novel routes of FSW for incorporating (a) GNPs; (b) Cu billets (All dimensions are in mm).

This study explores two novel approaches aimed at enhancing the weld strength of aluminum alloys through the integration of filler materials during FSW. In the first approach, 4 mm diameter cylindrical holes were drilled into the base plate, and GNPs were utilized as the filler material, illustrated in figure 4(a). The second approach involved drilling holes of 3 mm in diameter and 15 mm deep into the base plate in the transverse direction, with copper billets used as the filler material, as shown in figure 4(b). Additionally, tensile samples were prepared according to ASTM E08M specifications [28], as shown in figure 5. Three tensile test samples were used for each condition with a strain rate of 0.02 s^{-1}. A series of trial-and-error experiments were performed to determine the optimal process parameters for the FSW of the proposed materials. Various combinations of process parameters were tested, and significant FSW defects were noted, as illustrated in figure 6. However, using a tool rotational speed of 1200 rpm and a traverse speed of 31 mm min^{-1} resulted in defect-free joints. Consequently, the main FSW experiments were carried out with these parameters. The obtained FSWed joints are depicted in figure 7.

3. Results and discussion

3.1. Microstructure characteristics

SEM photomicrographs and EDS spectra of AA6082-T6/GNPs and AA6082-T6/Cu joint cross-sections are depicted in figures 8 and 9, respectively. In typical FSW joints, four distinct zones are identified, namely, the nugget zone (NZ), thermo-mechanically affected zone (TMAZ), heat-affected zone (HAZ), and base material (BM), illustrated in figures 7 and 8. In the microstructure of the base material zone, an area free of GNPs and the presence of precipitates is evident, as shown in figures 8(a) and 9(a). During the FSW process, the GNPs experience significant flow stress due to the stirring action of the tool, leading to their uniform distribution within the weld nugget, as observed in figure 8(c). The presence of GNPs within the weld nugget region is

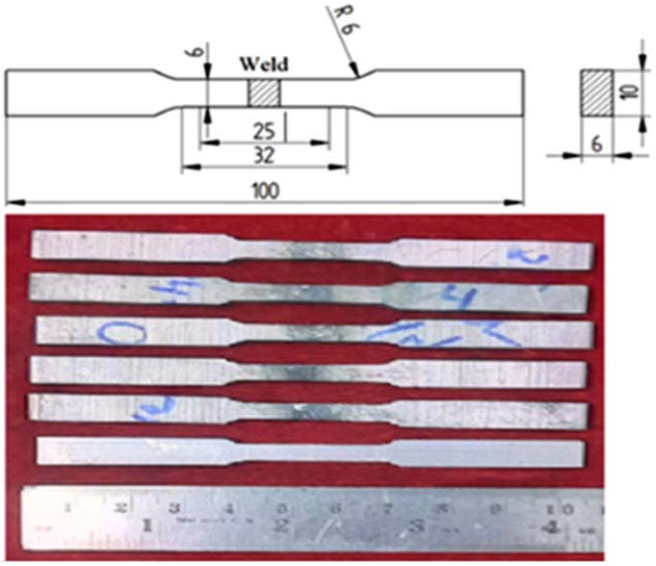

Figure 5. Tensile test specimens as per ASTM E08M (All dimensions are in mm).

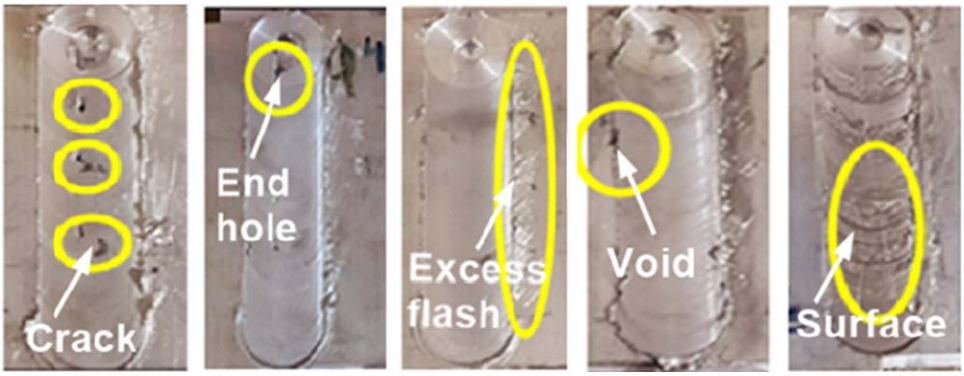

Figure 6. Various defects are observed in weld joints.

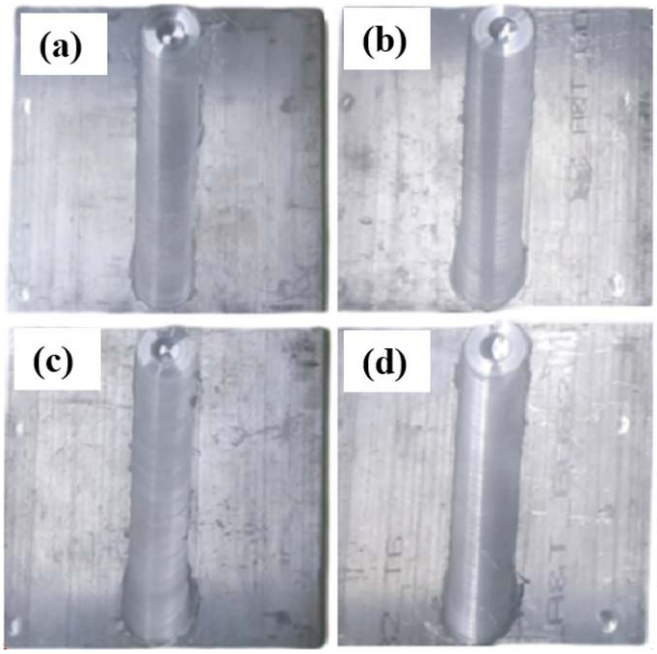

Figure 7. Fabricated FSW joints of (a) and (b) illustrates base material; (c) AA6082-T6/Cu joint; (d) AA6082-T6/GNPs joint.

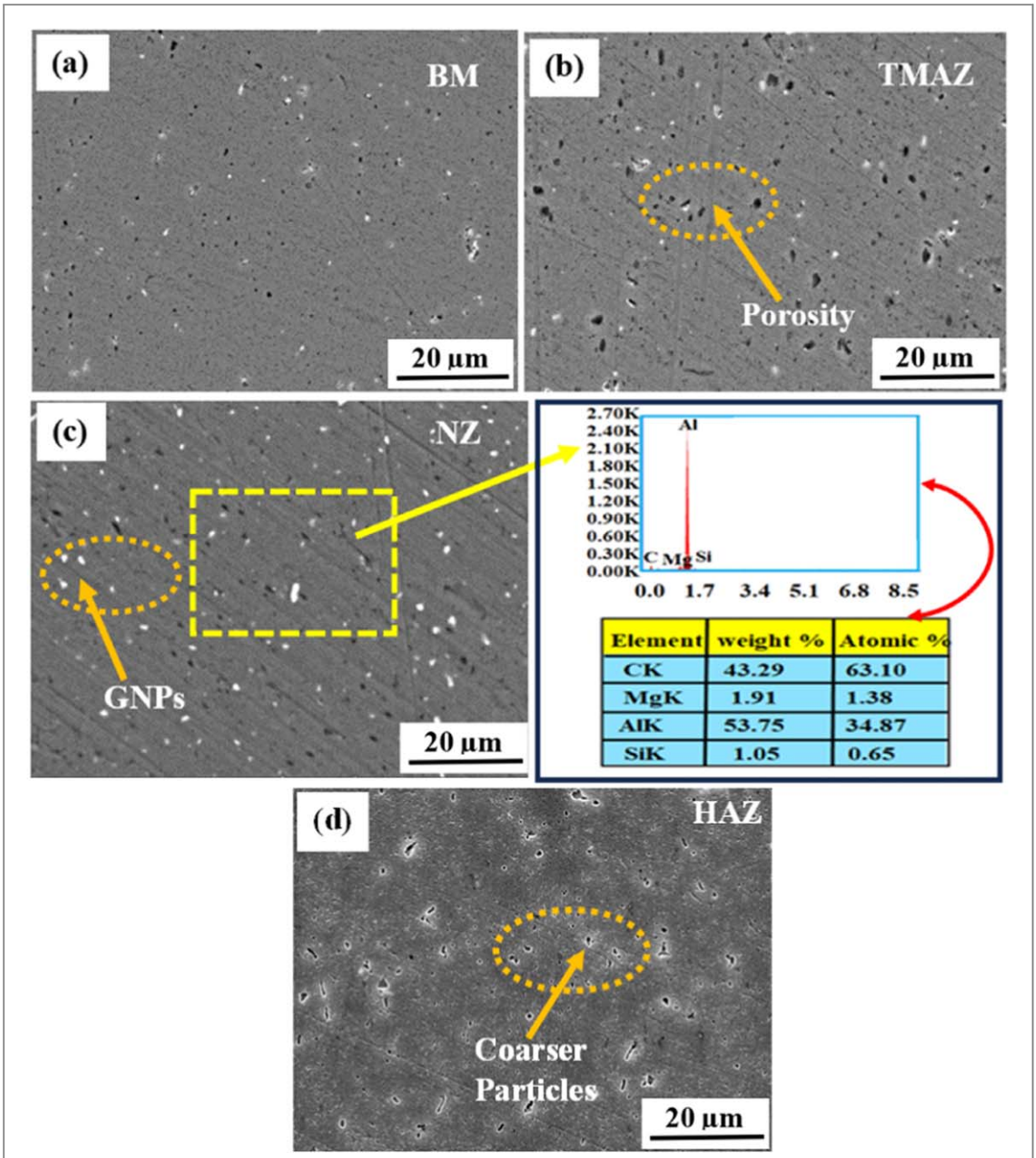

Figure 8. SEM/EDS photomicrographs of AA6082-T6/GNPs joint at (a) BM; (b)TMAZ; (c) NZ; (d) HAZ.

confirmed by EDS analysis. However, in HAZ, inadequate heat generation affects material plasticity, coarser grains, and the formation of porosity observed in figures 8(d) and 9(d).

The cross-section of AA6082-T6/Cu joint, the thermo-mechanically affected zone (TMAZ), reveals varying copper content, as depicted in figure 9(b), which is attributed to insufficient dynamic recrystallization (DRX). In the nugget zone, the EDS analysis confirms the presence of intermetallic compounds (IMCs), as shown in figure 9(c) [29]. The FSW joint demonstrates the presence of IMCs such as Al_2Cu_3, which contribute to bonding between the two alloys. Further, SEM micrographs, as depicted in figure 9(d), reveal small voids or cavities indicating porosity formation in the HAZ due to inadequate material flow or trapped gases.

Further, TEM micrographs of the FSW joint cross-section are depicted in figure 10, confirming the presence of GNPs in the nugget zone. The GNPs are composed of carbon atoms bound by relatively weak van der Waals forces and possess an interlayer shear strength of 0.47 MPa. Aluminum exhibits a higher interlayer shear strength than GNPs, aiding in achieving the critical threshold of 0.47 MPa during plastic deformation [30], thereby facilitating better integration of GNPs with aluminum, as shown in figure 10(a). The distinct boundaries between matrix and GNPs reinforcement are observed. Fine-sized GNPs are predominantly found in NZ. Moreover, the precipitates are also observed in aluminum alloy. Similarly, figure 10(b) reveals the presence of precipitates observed in the edge dislocation.

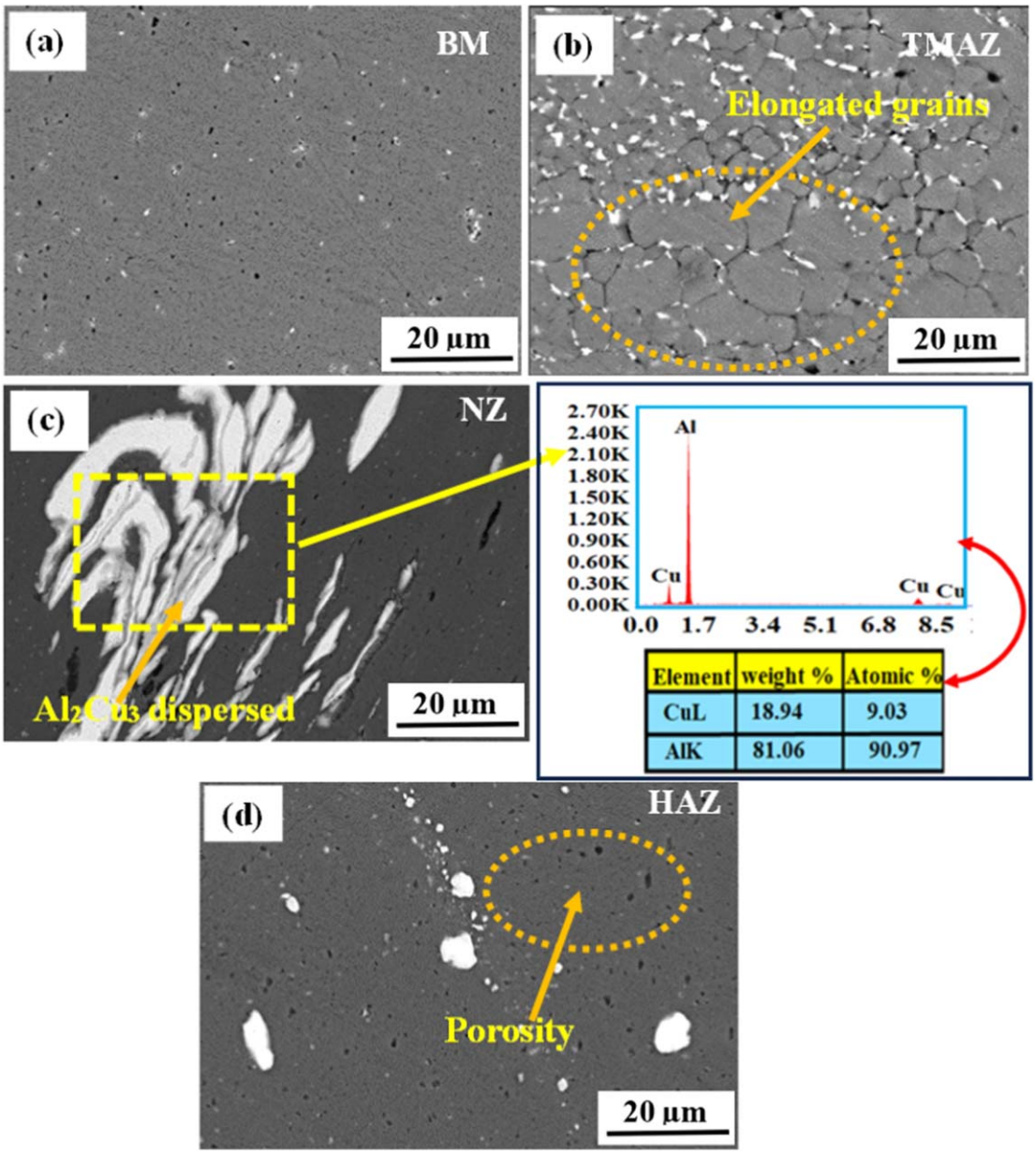

Figure 9. SEM/EDS photomicrographs of AA6082-T6/Cu joints at (a) BM; (b)TMAZ; (c) NZ; (d) HAZ.

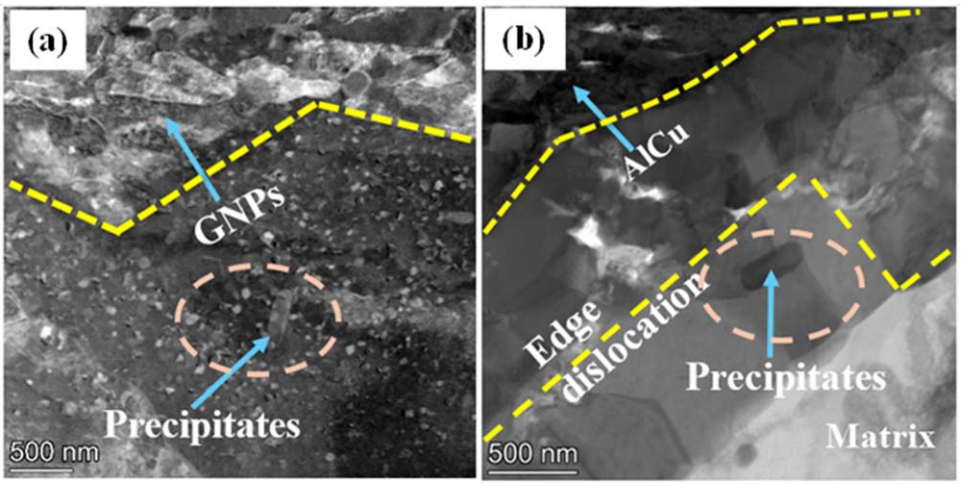

Figure 10. TEM bright field images of the interface region illustrate (a) AA6082-T6/GNPs joint; (b) AA6082-T6/Cu joint.

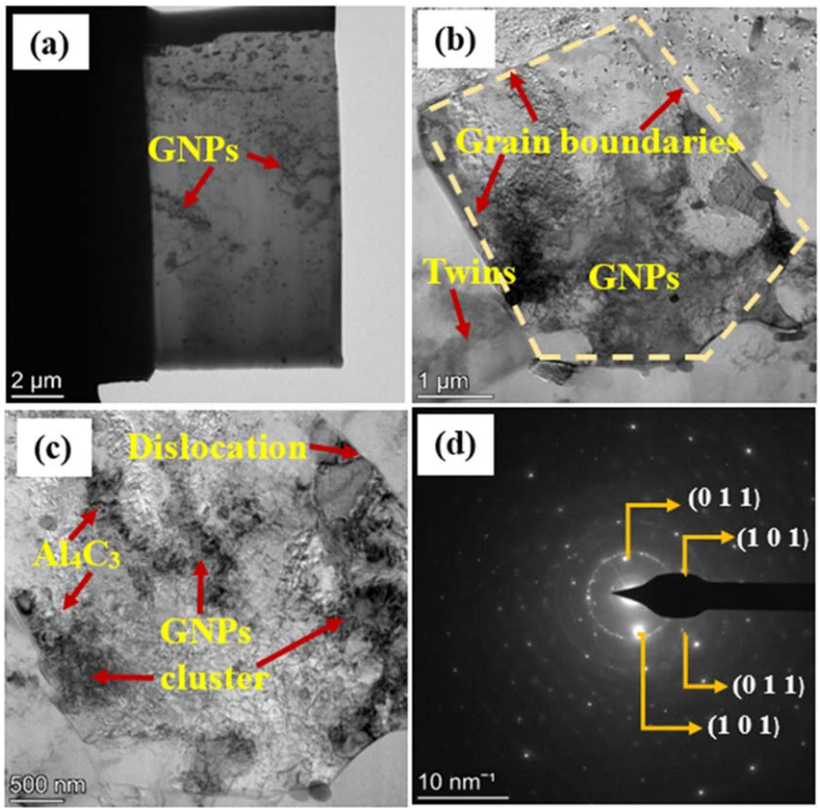

Figure 11. Bright-field TEM images of AA6082-T6/GNPs joint. (a) and (b) illustrate the presence of GNPs at grain boundaries; (c) formation of high energy dislocation; (d) HRTEM with SAED patterns for FCC grains.

Bright-field TEM images of AA6082-T6/GNPs and AA6082-T6/Cu joints are exhibited in figures 11 and 13, respectively. Figure 11(a) illustrates the dispersion of GNPs. In contrast, figure 11(b) shows GNPs embedded along the grain boundaries, induced by high-density dislocation due to varying coefficient of expansion between the aluminum alloy and GNPs. The grain refinement mechanism contributes to alloy strengthening, facilitated by the pinning effect caused by GNPs nucleation [18, 31]. High-resolution TEM (HRTEM) observation analyzes the nanocluster of GNPs. Figure 11(c) reveals high-density edge dislocations and slip planes (001) within face-centered cubic (FCC) grains, indicating nucleated dislocation. A selective area electron diffraction (SAED) pattern in figure 11(d) confirms the presence of FCC structures. The GNPs exhibit straight atomic layers (>50 layers) and are bonded with a semi-coherent structure in an aluminum interface and free from porosity or void in the formation of IMCs region [32]. Further, the elemental distribution was confirmed using a high-angle annular dark field (HAADF) image, as shown in figure 12 for AA6082-T6/GNPs joint exhibits elements like Al, Mg, Si, and C.

Effective dispersion of copper into aluminum alloy is evident, as depicted in figure 13(a), with a corresponding view of grains and grain boundaries shown in figure 13(b). Further, figure 13(c) illustrates the interface between the base material and nugget zone, highlighting the formation of Al_2Cu IMCs. The HRTEM imagery and SAED pattern are shown in figure 13(d). The elemental distribution map of FSWed joints reveals the presence of various elements such as Al, Mg, Si, C, Cr, Mn, K, Ti, Ni, and Cu [10, 33]. This elemental distribution was confirmed using a high-angle annular dark field (HAADF) image, as illustrated in figures 12 and 14 for AA6082-T6/GNPs and AA6082-T6/Cu joints, showing the presence of Al, Mg, Si, and Cu elements in the Cu added joint.

3.2. Microhardness characteristics

Vickers microhardness testing was conducted on the cross-section of FSWed joints. The base material exhibits a hardness of 109 HV. However, post-FSW, the hardness decreases due to thermal gradient variations. Figure 15 illustrates a typical 'W' shaped plot representing the hardness distribution across the FSWed joint. In the nugget zone, the hardness value effectively decreased due to the thermal softening of the material. The AA6082-T6/GNPs joint 66 HV and AA6082-T6/Cu joint 65 HV are achieved. These hardness results align closely with microstructural characteristics discussed in section 3.1. Similar findings were reported by Wang *et al* [22], which attributed to lower hardness in the nugget zone due to metallurgical transactions occurring in the nugget zone.

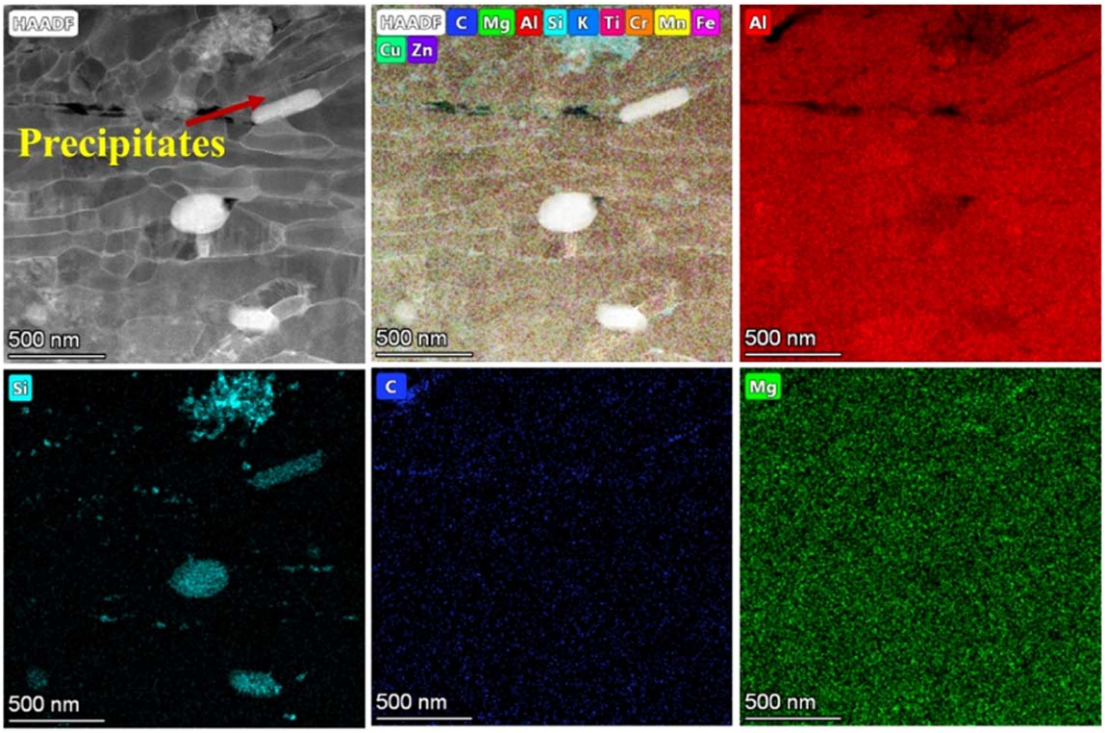

Figure 12. Elemental distribution map of AA6082-T6/GNPs joint.

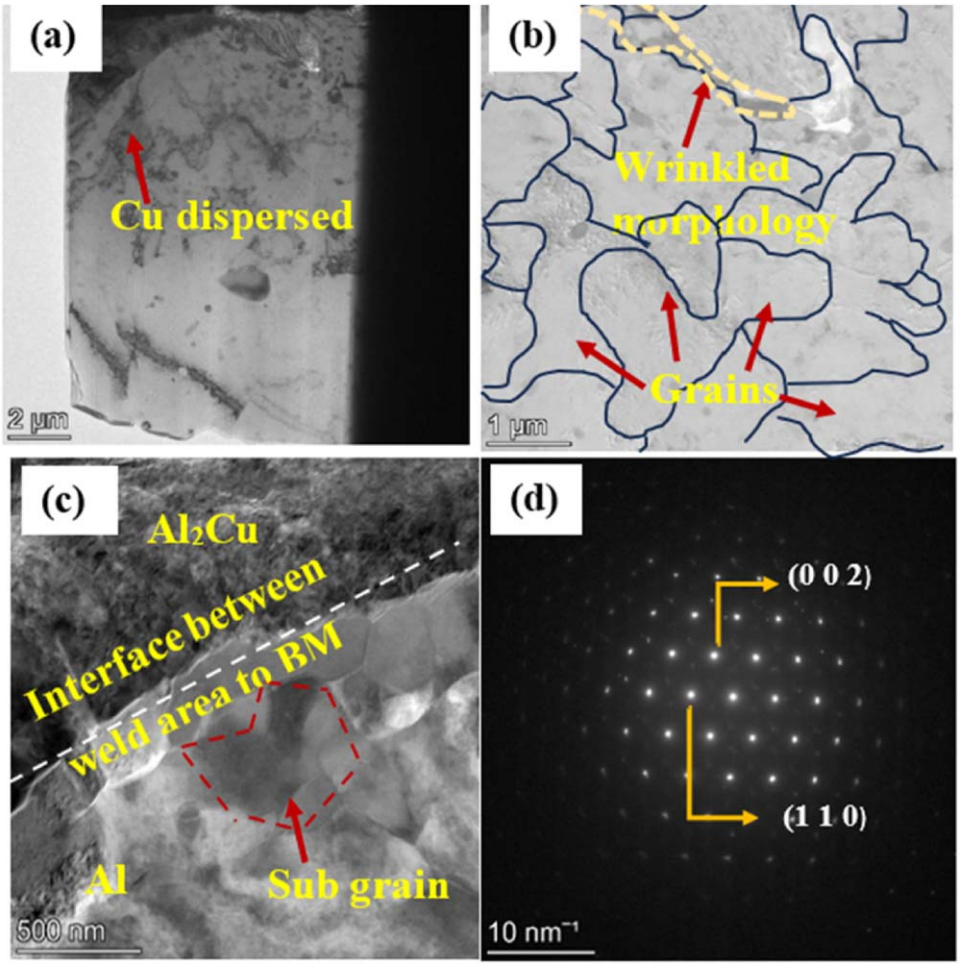

Figure 13. Bright field TEM images of AA6082-T6/Cu joint. (a) and (b) illustrate the grain boundaries and dispersion of Cu; (c) interface region between BM and NZ; (d) HRTEM image and SAED pattern for Al_2Cu.

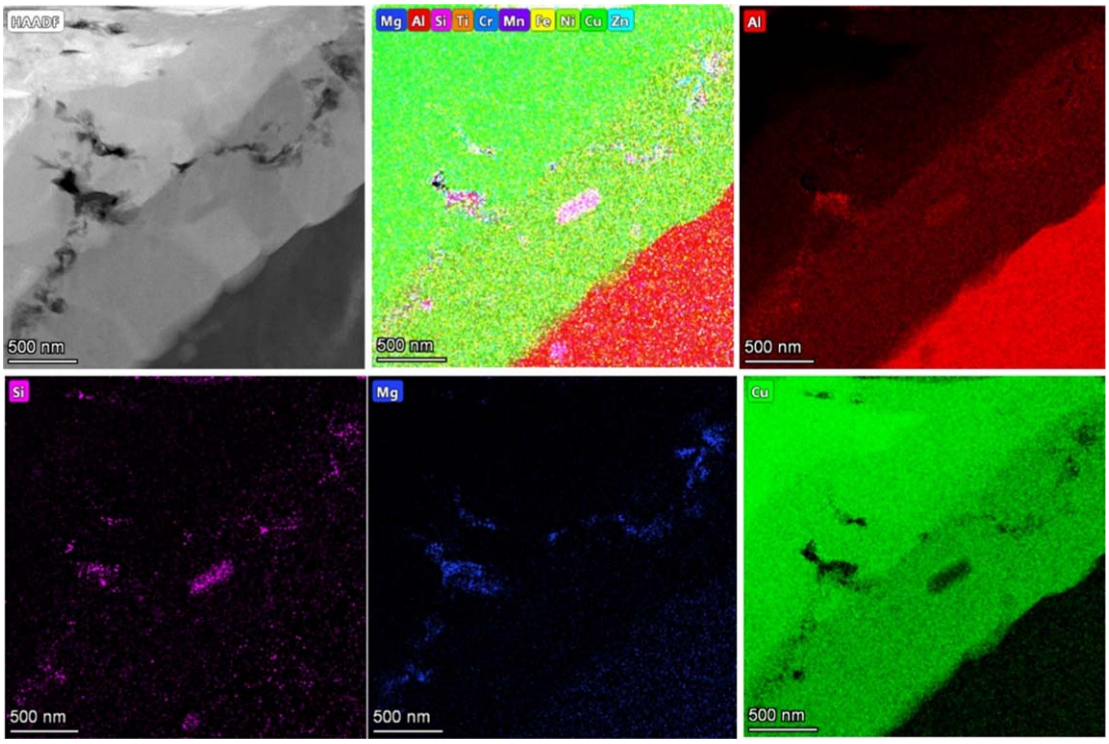

Figure 14. Elemental distribution map of AA6082-T6/Cu joint.

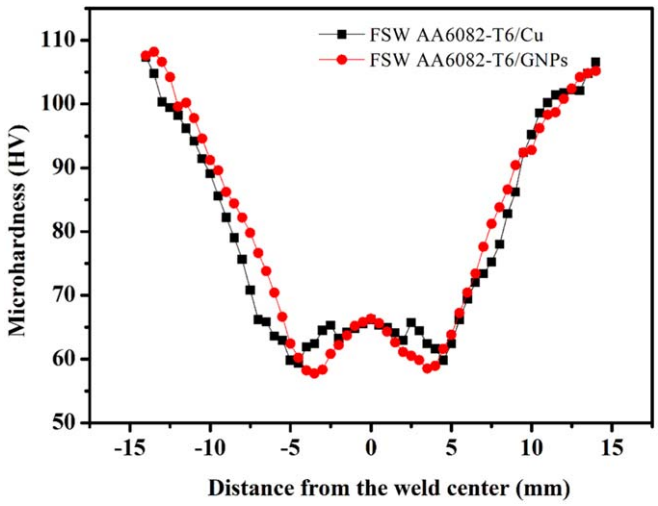

Figure 15. Microhardness in FSWed joint cross-section.

This led to sudden decreases in hardness as compared to base material. The severe plastic deformation induced by the stirring action of the FSW tool also contributes to the decreases in weld nuggets [10, 34].

3.3. Tensile characterization

The transverse tensile properties of FSWed joints were evaluated at room temperature using a computer-integrated universal testing machine (UTM). The study focused on determining the ultimate tensile strength (UTS) and yield strength (YS) of base material and FSWed joints. The stress–strain curve of different materials is depicted in figure 16. The FSWed joints exhibit lower strength compared to the base material due to the metallurgical transformation that occurs during the FSW process. The tensile properties correlate well with the microstructure and hardness characteristics of the joints, as shown in figures 8 and 9. The pinning effect of GNPs at grain boundaries exhibited in figure 11, contributed to increased YS and UTS, resulting in a 21%

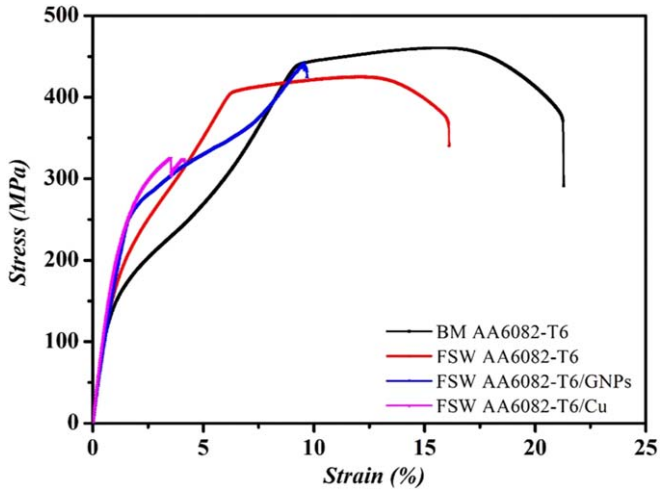

Figure 16. Engineering stress–strain diagram.

Table 3. Tensile properties of base material and FSWed joints.

Sample name	UTS (MPa)	Elongation (%)	Joint efficiency (%)
AA6082-T6	460	21.35	—
FSWed AA6082-T6	424	16.12	92.17
FSWed AA6082-T6/GNPs	412	9.8	89.56
FSWed AA6082-T6/Cu	316	4.6	68.69

improvement in joint efficiency for AA6082-T6/GNPs joints as compared to AA6082-T6/Cu joints. Fracture within the HAZ region indicates weaker strength formation due to coarser grain formation. Table 3 summarizes the tensile results and joint efficiency of base material and FSWed joints. Similar findings reported elsewhere indicate the enhanced strength due to uniform dispersion of GNPs and increased ductility due to good bonding between the aluminum and GNPs [32, 35].

3.4. Wear performance

The wear rate, coefficient of friction (COF), and frictional force of base material and FSWed joints were investigated using a pin-on-disc setup. The wear track diameter was maintained at 120 mm, and each test was performed for 10 min. Figure 17(a) depicts the wear behavior of base material and FSWed joints under a constant speed of 300 rpm across different loads ranging from 10 N to 40 N [36, 37]. The wear rate is increased for the AA6082-T6/Cu joint, from 38 μm to 13 μm due to material softening. In contrast, the base material AA6082-T6 exhibits a lower wear rate, reducing from 33 μm to 10 μm with increasing load from 10 N to 40 N; the GNPs-added joint produces a minimum wear rate compared to the Cu-added joint. Similar results were observed in AA7075/GNPs composites, where the wear rate and coefficient of friction (COF) decreased compared to the base material, attributed to the uniform dispersion of GNPs [38]. Researchers also noted improved wear resistance in AA6082 alloy with GNPs due to their even distribution [39].

A higher frictional force was observed in the AA6082-T6/Cu joint, increasing from 4.64 N to 13.79 N. In contrast, the AA6082-T6/GNPs joint and FSW AA6082-T6 exhibit frictional forces ranging from 3.63 N to 12.73 N and 2.99 N to 11.39 N, respectively, as depicted in figure 17(b). Similar results are reported in the FSW of AA6061/GNPs composites obtained for improved wear resistance [40]. The friction and wear characteristics of two-phase self-lubricating composites, such as Al/GNP composites, are complex and dependent on the applied load. The wear rate gradually decreases for FSWed AA6082-T6 and base material from 36 μm to 12 μm and 33 μm to 10.9 μm, respectively. Likewise, the AA6082/Graphene composite shows a reduction in wear rate, which is due to the self-lubricating properties of graphene [41]. The AlSi18CuNiMg alloy, reinforced with GNPs and CNTs, demonstrated improved wear performance attributed to the better dispersion of the carbonaceous reinforcements [42].

Figures 18(a)–(d) depict the COF values over time for base material and FSWed joints. Whereas Figures 19(a)–(b) present the average specific wear rate and COF values. These COF curves illustrate the evolution of COF during dry sliding tests. Initially, base material and FSWed AA6082-T6 samples exhibit high

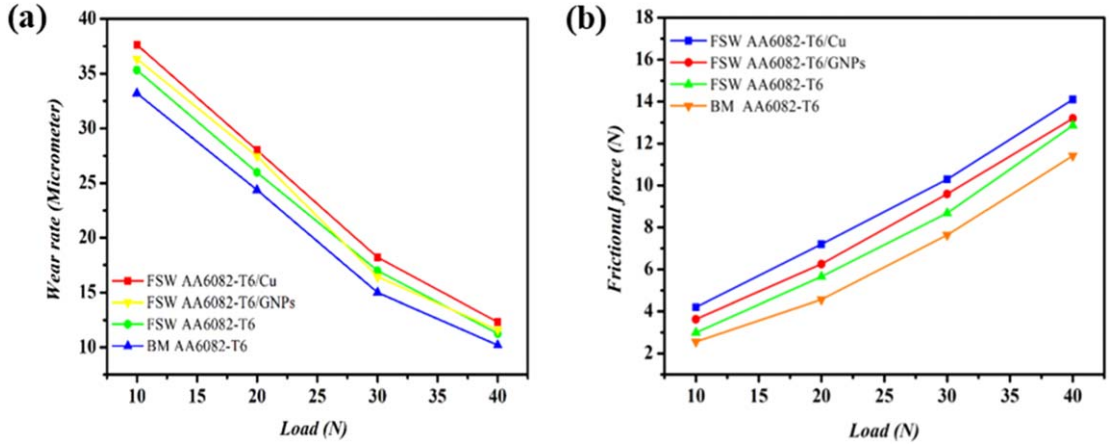

Figure 17. Graphs showing for a constant speed of 300 rpm. (a) Wear rate versus load; (b) frictional force versus load.

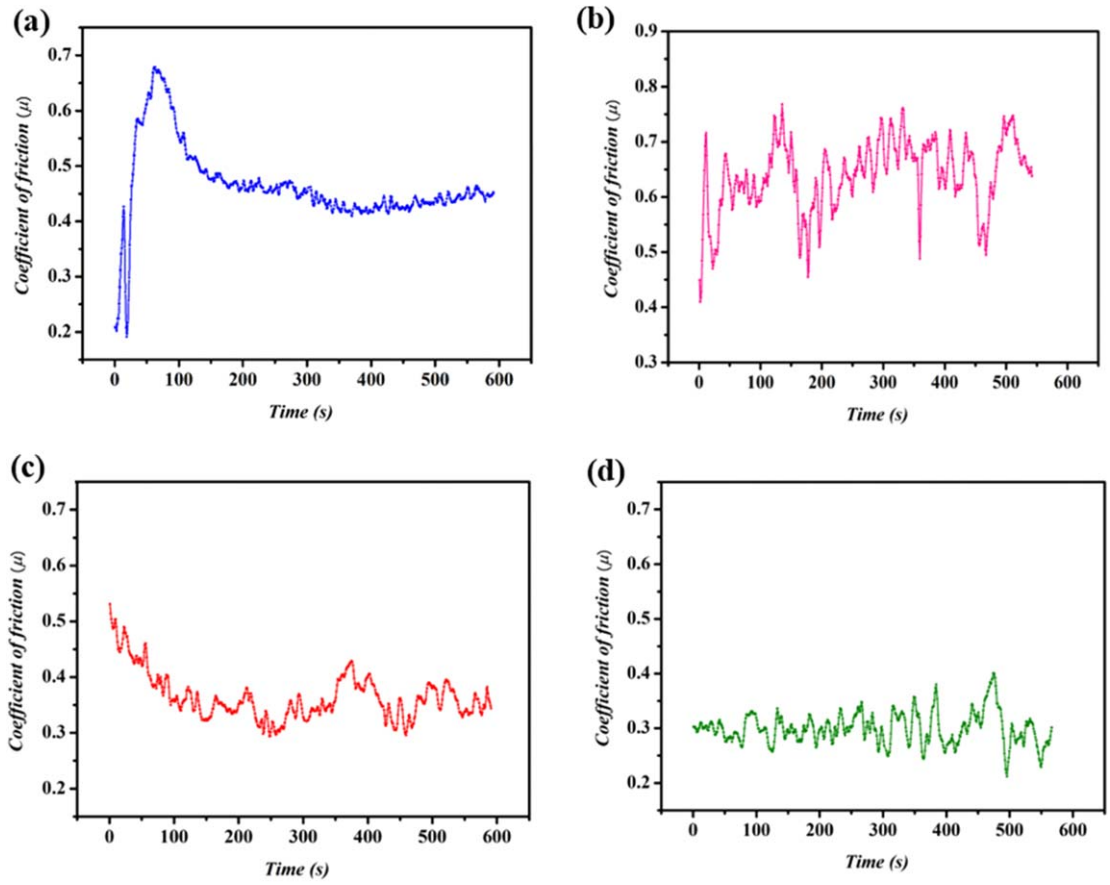

Figure 18. Coefficient of friction for (a) AA6082-T6; (b) FSW AA6082-T6; (c) FSW AA6082-T6/Cu; (d) FSW AA6082-T6/GNPs.

COF values. Over time, the COF gradually decreases, stabilizing joints with added GNPs and Cu. The COF maximum for the FSWed AA6082-T6 joint represents 0.75, whereas the base material produces a lower COF of 0.68. It's attributed to the increased incorporation of GNPs in aluminum, which leads to a reduction in microhardness.

3.5. Electrochemical analysis

The electrochemical characteristics of base material and FSWed joints were investigated at room temperature using the following techniques: open circuit potential (OCP), anodic polarization, and electrochemical impedance spectroscopy (EIS). These methods were employed to elucidate the electron charge transfer

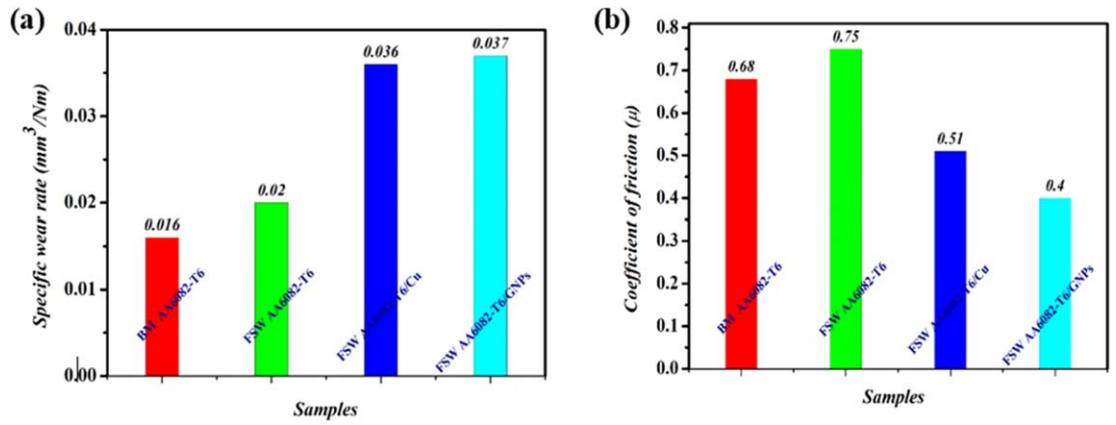

Figure 19. Variation of (a) specific wear rate; (b) the average COF values of various samples.

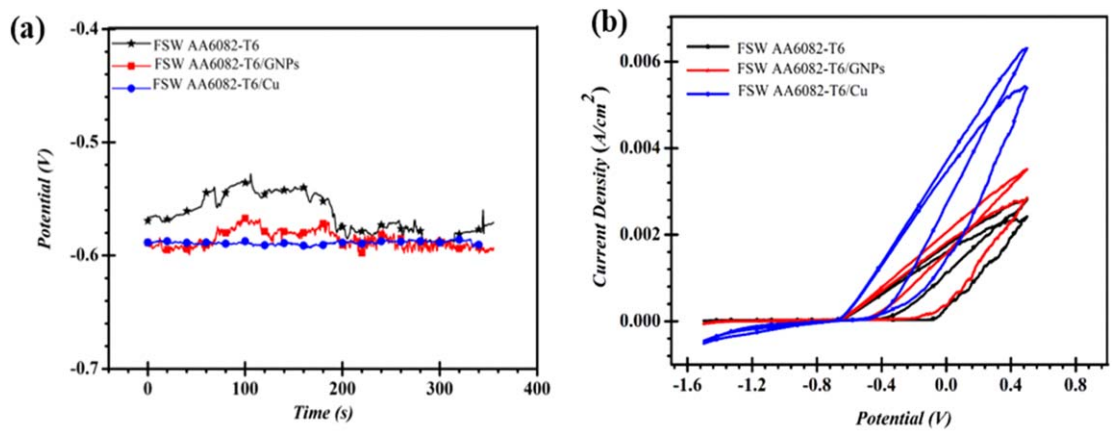

Figure 20. (a) Variation of OCP versus time curves in 3.5 wt% NaCl; (b) cyclic voltammograms curve.

mechanisms in the presence of a liquid electrolyte solution [43]. The formation of anodic and cathodic surfaces plays a crucial role in influencing the corrosion rate. Advanced microscopic probing techniques coupled with electrochemical impedance and polarization provide valuable insights into localized corrosion phenomena.

3.5.1. Open circuit potential (OCP) and potentiodynamic measurements

The FSW samples were utilized as working electrodes, and tests were conducted on 3.5 wt% of NaCl solution at 25 °C [44]. The variation of open circuit potential (OCP) over time is illustrated in figure 20(a). Upon immersion in the electrolyte solution, the corrosive effect of the salt solution becomes evident for both AA6082-T6/GNPs and AA6082-T6/Cu joints. Lower OCP values were observed in FSWed joints as compared to base material AA6082-T6. The AA6082-T6/Cu joint exhibits a stable potential value compared to AA6082-T6 and AA6082-T6/GNPs joints. This indicates that a better corrosion resistance of the AA6082-T6/Cu joint is formed. Potentiodynamic anodic polarization was performed starting from OCP to assess the polarization behavior, corrosion potential (Ecorr), and current density (Icorr) of each sample. Figure 20(b) displays the cyclic voltammogram curve, covering a potential range from −1.56 to 0.4 V. During anodic polarization, the faradaic current increased exponentially with rising anodic potential, indicating increased oxidation current. The E_{corr} value is higher for AA6082-T6/Cu and lower for FSWed AA6082-T6, suggesting that AA6082-T6/Cu is more susceptible to oxidative dissolution in the neutral electrolyte solution. However, FSWed AA6082-T6 and AA6082-T6/GNPs joints exhibit good corrosion resistance.

Specifically, the AA6082-T6/Cu joint shows a relatively high corrosion current of 5.2×10^{-3} A cm^{-2} at 0.4 V. Similarly, the AA6082-T6/GNPs joint exhibits a corrosion current of 3.1×10^{-3} A cm^{-2} at 0.4 V, while FSWed AA6082-T6 produces a corrosion current of 2.8×10^{-3} A cm^{-2} at 0.4 V.

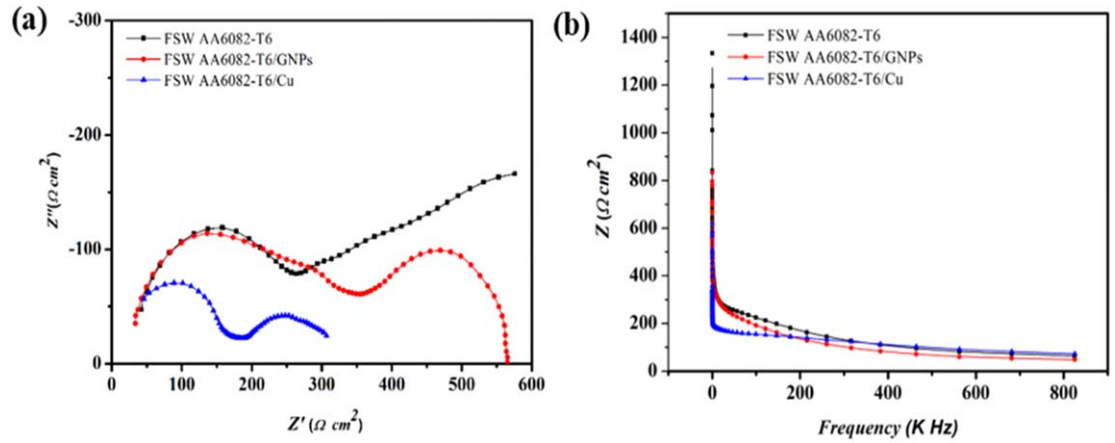

Figure 21. (a) EIS Nyquist plot; (b) Bode plot for AA6082-T6, AA6082-T6/GNPs, and AA6082-T6/Cu joint.

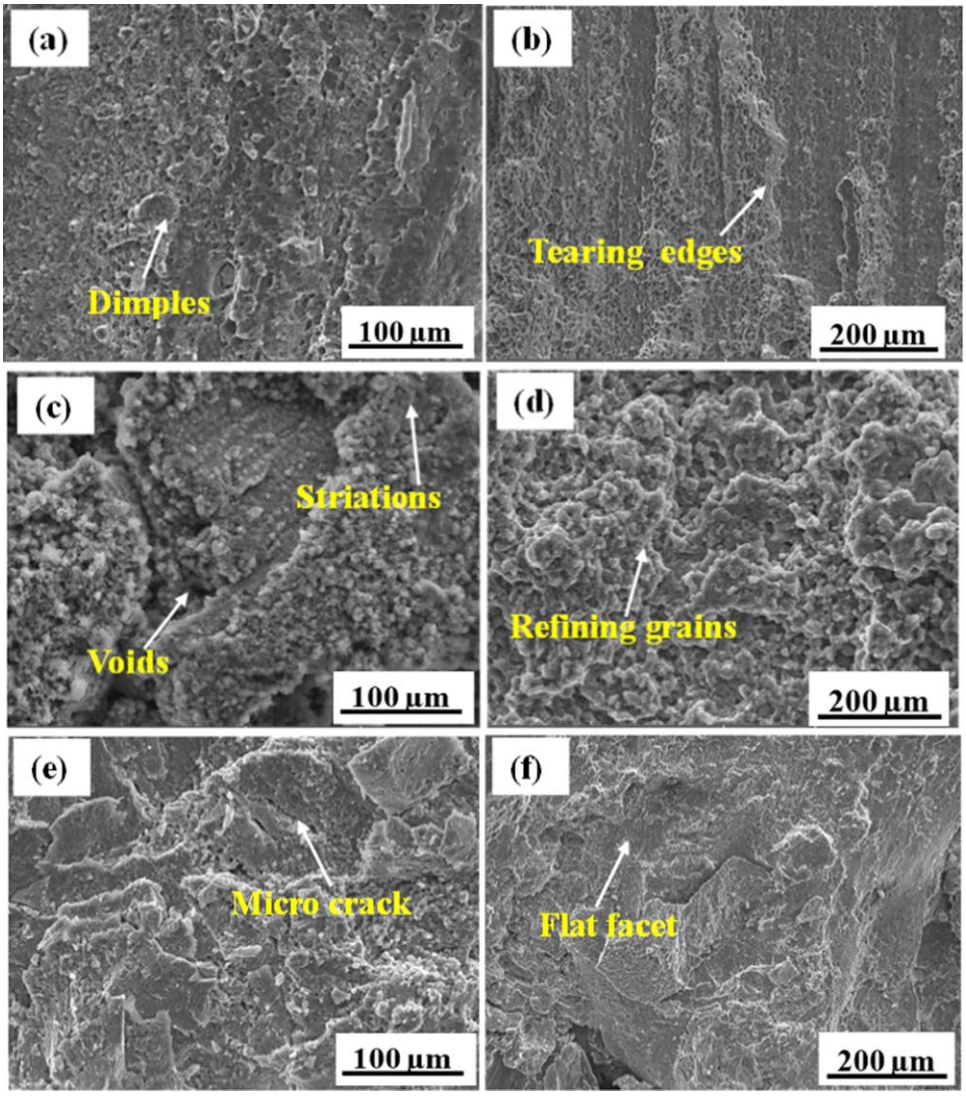

Figure 22. Fractography images of (a) and (b) base material; (c) and (d) AA6082-T6/GNPs joint; (e) and (f) AA6082-T6/Cu joint.

3.5.2. Electrochemical impedance spectroscopy (EIS) analysis.

This technique was employed to evaluate the corrosion resistance of AA6082-T6, AA6082-T6/GNPs, and AA6082-T6/Cu joints using a three-electrode cell configuration. Impedance frequencies were analyzed at a

corrosion potential of −0.4 V, which significantly influences interfacial charge transfer and surface stability in both base material and FSWed samples. The Electrochemical Impedance Spectroscopy (EIS) Nyquist plots are shown in figure 21(a). It exhibits higher frequencies indicative of interfacial charge transfer under constant phase elements [45]. The base material exhibits a higher curvature at high frequencies due to its greater surface roughness. The sequence of curvature diameters in the Nyquist plot is AA6082-T6/Cu joint » AA6082-T6/GNPs joint > FSWed AA6082-T6, reflecting varying charge transfer resistances to corrosion. AA6082-T6/GNPs show less corrosion resistance than AA6082-T6/Cu joint, with less effective interfacial charge transfer but good corrosion stability. Additionally, Bode plots shown in figure 21(b) indicate the corrosion layer forms homogeneously on the surface of FSWed joints but it is less resistant than the base material.

3.6. Fractography analysis

SEM fractography of the base material and FSWed joint is depicted in figure 22. The base material and reinforced GNPs joint exhibit a ductile mode of fracture. Figures 22(a)–(b) show dimples and tearing edges of ductile fractures. Further, the GNPs added joint exhibits dimples in fine-sized and small microvoids that are evident on the crack surface of the joint, as illustrated in figures 22(c)–(d). The occurrence of these dimples indicates the enhancement in ductility of the weld joints and better flow of the plasticized material [46]. Fracture of the tensile specimens occurred in the heat-affected zone (HAZ), which is a weaker area, as shown in figures 22(e)–(f). In contrast, figure 22(e)-(f) illustrates microcracks and pore formation in copper-added joints. The presence of flat facets with relative dimples suggests a brittle mode of fracture in the nugget region [47].

4. Conclusions

In conclusion, friction stir welding has proven effective in achieving robust joints in both AA6082-T6/GNPs and AA6082-T6/Cu materials. The innovative welding approaches employed in this study have resulted in improved joint characteristics. Particularly, AA6082-T6 joints reinforced with GNPs demonstrate higher weld hardness and joint efficiency than their counterparts, benefiting from the superior properties and effective bonding of GNPs with aluminum. The weld nugget exhibits a uniformly distributed graphene platelet structure facilitated by the stirring action of the FSW tool, enhancing material flow and increasing wear resistance in AA6082-T6/GNPs joints. Additionally, electrochemical corrosion studies indicated stable potential values for AA6082-T6/Cu joints. The proposed method of incorporating GNPs along the FSW line has led to a 21% enhancement in the weld strength of AA6082-T6. This novel welding technique holds promise for the welding industry in achieving superior FSW joints for various aluminum alloys.

Acknowledgments

The author(s) would like to acknowledge the REVA University, Bengaluru, India, for funding and research facilities [Ref No: RU: EST: ME: 2022–1] and CeNSE, IISc Bangalore, India, for experimental support. Filipe Fernandes acknowledges the UIDB/00285/2020 and LA/P/0112/2020 projects, sponsored by FEDER Funds through Portugal 2020 (PT2020), the Competitiveness and Internationalization Operational Program (COMPETE 2020), and national funds through the Portuguese Foundation for Science and Technology (FCT).

Data availability statement

All data that support the findings of this study are included within the article (and any supplementary files).

Authors contributions

R Biradar: Conceptualization, Methodology, Data Collection, Experimentation & Writing—Draft Manuscript; S Patil: Validation, Data Analysis & Interpretation, Writing—Manuscript, and Supervision; P Sharma: Visualization, Formal Analysis, Manuscript Review; F Fernandes: Formal Analysis, and Funding Acquisition.

Competing interests

The authors declare no competing interests that could influence the research work reported in this paper.

ORCID iDs

Rahul Biradar https://orcid.org/0000-0002-6128-9165
Sachinkumar Patil https://orcid.org/0000-0003-3391-0820
Priyaranjan Sharma https://orcid.org/0000-0002-0312-1612
Filipe Fernandes https://orcid.org/0000-0003-4035-3241

References

[1] Md Syam H, Tien W, Pradeep R and Michael N 2022 Analysis of the friction and wear of graphene reinforced aluminum metal matrix composites using machine learning models *Tribol. Int.* **170** 107527
[2] Hanliang L, Yanlong C, Ning L, Jinxiang W and Xiaojie L 2022 Phase constitution and texture distribution in the vortex zone of Co/Cu explosive welded plates *Journal of Material Research and Technology* **18** 4228–35
[3] Sasikumar A, Gopi S and Dhanesh G M 2021 Effect of welding speed on mechanical properties and corrosion resistance rates of filler induced friction stir welded AA6082 and AA5052 joints *Mater. Res. Express* **8** 066531
[4] SatishKumar T, Shalini S and Krishna K 2020 Effect of friction stir processing and hybrid reinforcement on wear behaviour of AA6082 alloy composite *Mater. Res. Express* **7** 026567
[5] Sindhuja M, Neelakrishnan S and Benjamin S D 2021 Friction stir welding parameters and their influence on mechanical properties of welded AA6061 and AA5052 aluminium plates *Mater. Res. Express* **8** 106525
[6] Yunqiang Z, Jiaqing Y, Jiachen Q, Chunlin D, Li L, Zhe L and Shu M 2022 Stationary shoulder friction stir welding of Al–Cu dissimilar materials and its mechanism for improving the microstructures and mechanical properties of joint *Mater. Sci. Eng.* A **837** 142754
[7] Luyao W H, Chenglong L, Yongyi G and Chenhui C 2019 Influences of work hardening and crystallographic texture on dry sliding tribological properties of friction stir processed pure Ti with slow rotation speed *Mater. Res. Express* **6** 0865c9
[8] Fei Q, Shewei X, Xingyang T, Huan W, Ping G, Hongmiao H, Zhiwei L, Lei Z and Wentao H 2024 Low-temperature superplastic deformation mechanism of ultra-fine grain Ti–6Al–4V alloy by friction stir processing *Journal of Materials Research and Technology* **30** 7413–9
[9] Sachinkumar P, Narendranath S and Chakradhar D 2020 Characterization and evaluation of joint properties of FSWed AA6061/SiC/FA hybrid AMCs using different tool pin profiles *Trans. Indian Inst. Met.* **73** 2269–79
[10] Giorgi M, Scialpi A, Panella F W and Filippis L A C 2009 Effect of shoulder geometry on residual stress and fatigue properties of AA6082 FSW joints *J. Mech. Sci. Technol.* **23** 26–35
[11] Yuming X, Xiangchen M, Yongxian H, Junchen L and Jian C 2019 Deformation-driven metallurgy of graphene nanoplatelets reinforced aluminum composite for the balance between strength and ductility *Composites* B **177** 107413
[12] Sachinkumar P, Narendranath S and Chakradhar D 2019 Microstructure, hardness and tensile properties of friction stir welded aluminum matrix composite reinforced with SiC and Fly ash *Silicon* **11** 2557–65
[13] Shokrieh M, Esmkhani M, Shahverdi R and Vahedi F 2013 Effect of graphene nanosheets (GNS) and graphite nanoplatelets (GNPs) on the mechanical properties of epoxy nanocomposites *Science of Advanced Materials* **5** 1–7
[14] Mahmood K, Rafi U, Abdul W, Wilayat H, Shahid A and Ragnhild E 2019 Effect of graphene nanoplatelets on the physical and mechanical properties of Al6061 in fabricated and T6 thermal conditions *J. Alloys Compd.* **790** 1076–91
[15] Saurabh D, Avik M, Roy M, Satish V and Chattopadhyay K 2018 Multi-layer graphene reinforced aluminum—Manufacturing of high strength composite by friction stir alloying *Composites* B **136** 63–71
[16] Abhishek S, Vyas S, Agam G, Pragya R, Surja P and Jinu P 2020 Friction stir lap welding of AA6061 aluminium alloy with a graphene interlayer *Materials and Manufacturing Process* **35** 258–69
[17] Huijie Z, Xu L, Baoxin Z and Yang G 2022 Enhancing the mechanical performances of friction stir lap welded Al-Zn-Mg-Cu alloy joint by promoting diffusion of alloying element Zn toward the pre-positioned Cu interlayer *Mater. Sci. Eng.* A **832** 142467
[18] Sunil R, Tanmoy D, Ajay M S and Jinu P 2022 Fabrication and characterization of Al/GNPs composite by bottom pouring stir casting *Mater. Lett.* **327** 133002
[19] Yijun L, Gaoqiang C, Hua Z, Chengle Y, Shuai Z, Qu L, Mengran Z and Qingyu S 2021 *In situ* exfoliation of graphite for fabrication of graphene/aluminum composites by friction stir processing *Mater. Lett.* **301** 130280
[20] SungT H, Hrishikesh D, Hyun-S O, Mohammad N and Doo M C 2017 Combination of nano-particle deposition system and friction stir spot welding for fabrication of carbon/aluminum metal matrix composite joints of dissimilar aluminum alloys *CIRP Ann.* **66** 261–4
[21] Khodabakhshi F, Nosko M and Gerlich A P 2018 Effects of graphene nano-platelets (GNPs) on the microstructural characteristics and textural development of an Al-Mg alloy during friction stir processing *Surface and Coating Technology* **335** 288–305
[22] Shuai W, Xiao W, Jijin X, Jie H, Xuefeng S, Chun Y, Junmei C, Xiaoqi C and Hao L 2020 Strengthening and toughening mechanisms in refilled friction stir spot welding of AA2014 aluminum alloy reinforced by graphene nanosheets *Mater. Des.* **186** 108212
[23] Mohammad S M I, Mohd R M, Farazila Y, Nukman Y, Zbigniew B, Tetsuo S, Yoshiaki M and Hidetoshi F 2023 Improved mechanical and electrical properties of copper-aluminum joints with highly aligned graphene reinforcement via friction stir spot welding *Journal of Material Research and Technology* **24** 9203–15
[24] Sinha V C, Kundu S and Chatterjee S 2016 Microstructure and mechanical properties of similar and dissimilar joints of aluminium alloy and pure copper by friction stir welding *Perspective in Science* **8** 543–6
[25] Felix X M and Jayabalan V 2015 Tool travel speed effects on the microstructure of friction stir welded aluminum–copper joints *J. Mater. Process. Technol.* **217** 105–13
[26] Carvalho G H S F L, Galvão I, Mendes R, Leal R M and Loureiro A 2019 Friction stir welding and explosive welding of aluminum/copper: process analysis *Mater. Manuf. Processes* **34** 1243–50
[27] Galvao I, Oliveira J C, Loureiro A and Rodrigues D M 2011 Formation and distribution of brittle structures in friction stir welding of aluminium and copper influence of process parameters *Sci. Technol. Weld. Joining* **16** 681–9
[28] Sachinkumar P, Narendranath S and Chakradhar D 2018 Process parameter optimization for FSW of AA6061/SiC/fly ash AMCs using Taguchi technique *Emerging Materials Research* **7** 192–9
[29] Joanna W B, Natalia S, Lidia L D, Boguslaw O and Rafal N 2012 TEM characterization of the reaction products formed in Al–Cu/SiO_2 couples due to high temperature interaction *Journal of Material Science* **47** 8464–71

[30] Mostafa M, Aliasghar A, Mohadeseh P and Fariborz S 2021 The effect of polymeric surfactant content on the mechanical properties of Al/GNP nanocomposites *Mater. Chem. Phys.* **257** 126831
[31] Sathish T, Pratibha C, Mani P, Gangolu N R, Padmavathy S, Asiful H S and Abhishek G 2023 Maximizing machinability at AA8014 joints by hybrid reinforcement in friction stir processing *International Journal of Interactive Design and Manufacturing* **18** 4617–28
[32] Mahmood K, Rafiud D, Muhammad A B, Abdul W, Syed W H, Shahid A and Ragnhild A 2021 Effects of graphene nanoplatelets and boron carbide on microstructure and mechanical behaviour of aluminium alloy (Al6061) after friction stir welding *Advances in Materials and Processing Technology* **8** 3148–64
[33] Ajay P H C, Madhu, Abhishek P, Chandra S P, Satish V K, Uma G and Pradeep R 2020 Friction stir processing of squeeze cast A356 with surface compacted graphene nanoplatelets (GNPs) for the synthesis of metal matrix composites *Mater. Sci. Eng.* A **769** 138517
[34] Krishna K M and Kumar A 2018 Influence of ridges shoulder with polygonal pins on material flow and friction stir weld characteristics of 6082 aluminum alloy *J. Manuf. Processes* **32** 625–34
[35] Puzhen S, Wenshu Y, Qiang Z, Qingyu M, Xin T, Ziyang X, Jing Q, Zhenhe Y and Gaohui W 2018 Microstructure and tensile properties of 5083 Al matrix composites reinforced with graphene oxide and graphene nanoplates prepared by pressure infiltration method *Composites* A **109** 151–62
[36] Zhou Z, Jiang Z, Zheng Q, Li Y, Yuan Z, Ding C and Piao Z 2024 Research on the construction of gradient nanostructure and anti-tribo corrosion behavior of aluminum alloy surface *Tribol. Int.* **194** 109448
[37] Jian J, Wentao H, Xiaomei F and Yifu S 2023 Oxidation resistant FeCoNiCrAl high entropy alloy/AlSi12 composite coatings with excellent adhesion on Ti-6Al-4 V alloy substrate via mechanical alloying and subsequent laser cladding *Surface and Coating Technology* **464** 129577
[38] Ragu S, Suganeswaran K, Surya K, Thangavel P and Gobinath V K 2023 Investigations on microstructure, thermo-mechanical and tribological behaviour of graphene oxide reinforced AA7075 surface composites developed via friction stir processing *Journal of manufacturing process* **90** 139–50
[39] Maheswara R, Durga K G and Venkata S K 2024 Multi-criteria optimization for wear and friction properties of self-lubricating Al6082-T6/GNP/TiB_2 hybrid composites *Journal of the Institution of Engineers (India) Series* D **8** 3148–64
[40] Abhishek S, Damanapeta N V M, Baidehish S and Jinu P 2019 Surface modification of Al6061-SiC surface composite through impregnation of graphene, graphite & carbon nanotubes via FSP: a tribological study *Surface and Coating Technology* **368** 175–91
[41] Sreehari P, Muthu V A and Raghuraman S 2020 Tribological study of graphene reinforced AA6082 surface composite processed through friction stir processing *Material Today Proceedings* **27** 2225–9
[42] Muhammet E T, Fatih A, Yavuz S, Huseyin Z and Yuksel A 2021 Wear resistance and tribological properties of GNPs and MWCNT reinforced AlSi18CuNiMg alloys produced by stir casting *Tribol. Int.* **164** 107201
[43] Ali D, Zohreh E and Madjid S 2016 Microstructure and corrosion characterization of the interfacial region in dissimilar friction stir welded AA5083 to AA7023 *Corros. Sci.* **107** 133–44
[44] Patil H S and Soman S N 2014 Corrosion behaviour of friction stir welded aluminum alloys AA6082-T6 *American Journal of Materials Engineering and Technology* **2** 29–33
[45] Zhong Z, Yang Y, Jian Z and Xi W 2017 Corrosion behavior of keyhole-free friction stir spot welded joints of dissimilar 6082 aluminum alloy and DP600 galvanized steel in 3.5% NaCl Solution *Metals* **7** 338
[46] Nazari M, Eskandari H and Khodabakhshi F 2019 Production and characterization of an advanced AA6061-Graphene-TiB2 hybrid surface nanocomposite by multi-pass friction stir processing *Surface and Coating Technology* **377** 124914
[47] Zhang Z W, Liu Z Y, Xiao B L, Ni D R and Ma Z Y 2018 High efficiency dispersal and strengthening of graphene reinforced aluminum alloy composites fabricated by powder metallurgy combined with friction stir processing *Carbon* **135** 215–23